

The stellar and hot gas content of low-mass galaxy clusters

Michael L. Balogh¹, Pasquale Mazzotta^{2,3}, Richard G. Bower⁴, Vince Eke⁴,
Hervé Bourdin², Ting Lu¹, Tom Theuns^{4,5}

¹Department of Physics and Astronomy, University of Waterloo, Waterloo, Ontario, N2L 3G1, Canada

²Dipartimento di Fisica, Università degli Studi di Roma “Tor Vergata”, via della Ricerca Scientifica, 1, 00133 Roma, Italy

³Harvard-Smithsonian Center for Astrophysics, 60 Garden Street, Cambridge, MA 02138, USA

⁴Department of Physics, University of Durham, Science Laboratories, South Road, Durham DH13LE, UK

⁵Department of Physics, University of Antwerp, Campus Groenenborger, Groenenborgerlaan171, B-2020 Antwerp, Belgium

25 October 2018

ABSTRACT

We analyse the stellar and hot gas content of 18 nearby, low-mass galaxy clusters, detected in redshift space and selected to have a dynamical mass $3 \times 10^{14} < M/M_{\odot} < 6 \times 10^{14}$ ($h = 0.7$), as measured from the 2dF Galaxy Redshift Survey. We combine X-ray measurements from both *Chandra* and *XMM* with ground-based near-infrared observations from CTIO, AAT and CFHT to compare the mass in hot gas and stars to the dynamical mass and state of the clusters. Only 13 of the clusters are detected in X-ray emission, and for these systems we find that a range of 7–20 per cent of their baryonic mass, and < 3 per cent of their dynamical mass, is detected in starlight, similar to what is observed in more massive clusters. In contrast, the five undetected clusters are underluminous in X-ray emission, by up to a factor 10, given their stellar mass. Although the velocity distribution of cluster members in these systems is indistinguishable from a Gaussian, all show subtle signs of being unrelaxed: either they lack a central, dominant galaxy, or the bright galaxy distribution is less concentrated and/or more elongated than the rest of the sample. Thus we conclude that low-mass clusters and groups selected from the velocity distribution of their galaxies exhibit a dichotomy in their hot gas properties. Either they are detected in X-ray, in which case they generally lie on the usual scaling relations, or they are completely undetected in X-ray emission. The non-detections may be partly related to the apparently young dynamical state of the clusters, but it remains a distinct possibility that some of these systems are exceptionally devoid of hot emitting gas as the result of its expulsion or rarefaction.

Key words: galaxies: clusters

1 INTRODUCTION

Galaxy clusters and groups are important both as cosmological probes, and as laboratories for studying galaxy evolution. In particular, their deep gravitational potential means that their baryon content should be nearly representative of the Universe as a whole, and that the diffuse gas is at a temperature that is accessible to observation. As a result, they represent one of the few places where it is possible to study the stars, cold and hot gas, and dark matter in a single system.

It is now well known that the mass fraction in stars is not universal, but in general decreases with increasing cluster mass (e.g. Eke et al. 2004b, 2005; Ramella et al. 2004; Lin et al. 2003; Giodini et al. 2009). On the other hand, the mass fraction of hot gas appears to *increase* with mass (e.g. Vikhlinin et al. 2006; Sun et al. 2009; Pratt et al. 2010). If these systems are closed boxes, then the sum of stellar and gas mass fractions should equal the universal value $f_b = \Omega_b/\Omega_m$, where Ω_b and Ω_m are the baryon and

matter densities, respectively, relative to the critical density. Recently Gonzalez et al. (2007) claimed this to be the case, in particular arguing that in the lowest mass systems there is significant stellar mass in the intracluster-light and halo of the central galaxy, which completes the baryon fraction. The interpretation then is that most of the baryons in these low-mass groups have cooled to form stars; this poses a challenge for normal hierarchical models which predict that more massive clusters are actually built from these groups (Balogh et al. 2008). An important open question then is whether or not there really exists a significant population of groups with $M_{\text{stars}}/M_{\text{gas}} > 20$ per cent. The conclusions of Gonzalez et al. (2007) depend partly on an extrapolated mean relation for the gas fraction of clusters as a function of mass, taken from Vikhlinin et al. (2006). However, similar conclusions were reached by Laganá et al. (2008), based on a small sample of five nearby Abell clusters observed with *XMM*.

The other possible explanation for the high ratio of stellar-to-gas mass in groups is that these systems are deficient in X-

ray emitting gas, and associated metals. Recent observations by Giodini et al. (2009) and Rasmussen & Ponman (2009) indicate this is the case; in particular the latter provides an interesting analysis of the abundances in a sample of 15 X-ray bright groups (Rasmussen & Ponman 2007) and concludes that these groups have fewer metals than expected given their stellar mass. However, their sample was selected (from the larger sample of Osmond & Ponman 2004) to have relaxed X-ray morphologies and good photon statistics. They may therefore be biased toward undisturbed, cool-core groups which are unlikely to be the typical precursor of more massive clusters (Rasmussen & Ponman 2009). The apparent requirement for strong energy sources to counter the high cooling rates near the centre of clusters may provide a natural mechanism for removing hot gas from groups. Models incorporating supernova-driven superwinds (e.g. Davé et al. 2008a) or supermassive black hole accretion (e.g. Bower et al. 2008; McCarthy et al. 2010a) have had considerable success at matching the observed properties of X-ray emitting gas in groups and clusters. Alternatively, models in which gas was heated prior to the virialization of the group or cluster predict that such systems would fail to accrete their full complement of gas in the first place (e.g. Balogh et al. 1999; McCarthy et al. 2008).

Most of the work that has been done so far has been based on X-ray selected samples of clusters, which introduces a potential bias. Several investigations have been conducted in an attempt to evaluate the importance of this bias. In particular, Bower et al. (1994), Gilbank et al. (2004), Donahue et al. (2001), Popesso et al. (2007) and Rozo et al. (2009) make use of pointed and archival *ROSAT* observations of cluster samples, identified based upon their optical galaxy population using redshift and position information. All of these independent studies found significant scatter between the optical richness (or total optical luminosity) and X-ray luminosity of their systems. In particular, both Bower et al. (1997) and Rykoff et al. (2008a) find their optically-detected clusters are systematically underluminous in X-rays, relative to X-ray selected samples. Similar conclusions have been reached by Hicks et al. (2008), using *Chandra* observations of 13 optically-selected clusters at $0.6 < z < 1.1$. This is at least partly due to a Malmquist-type bias in X-ray flux limited surveys (Ikebe et al. 2002; Pratt et al. 2009; Vikhlinin et al. 2009); for example, Rykoff et al. (2008b) use weak-lensing based mass estimates to conclude that, once a correction is made for non-hydrostatic equilibrium and this Malmquist bias, the $L_X - M$ relation defined by their optically-selected clusters is similar to that of the X-ray selected HIFLUGCS (Reiprich & Böhringer 2002) sample.

Recently, Rasmussen et al. (2006) have begun an interesting study of a redshift-selected, unbiased group sample followed up with *XMM*. Of the first nine analysed, only three were detected, and two of these are underluminous given their velocity dispersion (Bai et al. 2010). Based on their velocity distribution, Rasmussen et al. (2006) argue that the underluminous systems are in the early stage of collapse; similar interpretations of such systems have been made by Popesso et al. (2007) and Dietrich et al. (2009).

What is clear is that the mass and dynamical state distribution of a cluster sample will be sensitive to the way the clusters are detected. It is important to understand these effects, both to identify robust indicators of a cluster's mass and to use them as cosmological probes. Perhaps even more interesting is the fact that the scatter in key properties such as gas entropy and stellar fraction, at fixed total mass, contains important information about the physical

processes associated with galaxy formation (e.g. McCarthy et al. 2010b; Davé et al. 2008b).

One of the most common ways to select groups and clusters from large redshift surveys is the friends-of-friends linking method, which has the advantage that it is easy to implement and fairly straightforward to calibrate with numerical simulations (e.g. Eke et al. 2004a). Eke et al. (2005) used such a sample from the 2dFGRS (Colless et al. 2001) to demonstrate that most of the stars in the Universe are associated with small groups, $M \sim 2 \times 10^{12} M_\odot$, in reasonable agreement with model predictions (Bower et al. 2006). It would be of interest to know the fate of the hot gas in groups selected in this way: in particular, what is the efficiency of converting gas to stars on average, and what is its variation between systems?

We have therefore selected 18 low-mass clusters, with $3 \times 10^{14} < M/M_\odot < 6 \times 10^{14}$, from the catalogue of Eke et al. (2004a). All but two of the 18 clusters were followed up with pointed *Chandra* or *XMM* observations. This represents the first time that a complete, optically-selected sample of low-mass clusters has been followed up with these facilities. Surprisingly, we found that despite the narrow selection on dynamical mass, the clusters have a wide range of X-ray luminosities, and five of them were undetected. The details of the object selection and X-ray observations are given in Mazzotta et al. (in prep, hereafter Paper II). Here we present an analysis of near-infrared (NIR) data in these clusters, to measure the stellar luminosity and mass. The plan of the paper is as follows. The origin and reduction of the NIR data is described in § 2. The details of the photometry and calculation of NIR luminosity are given in § 3. We then calculate the total NIR luminosity of each cluster and consider various scaling relationships with dynamical and X-ray properties, in § 4. We find that most of the clusters appear normal when compared with X-ray selected samples; we explore possible explanations for the five undetected clusters in § 5, finally drawing our conclusions in § 6.

We use a cosmology with $\Omega_m = 0.3$, $\Omega_\Lambda = 0.7$ and $h = H_0/(100\text{km/s/Mpc}) = 0.7$. All NIR magnitudes are on the Vega (2MASS) system.

2 OBSERVATIONS

2.1 Cluster selection

We selected 18 clusters from the catalogue of Eke et al. (2004a); the adopted centres and redshifts, which in some cases differ from those in the original catalogue, are given in Table 1. Our main aim was to look for the variation in X-ray emission from a mass-selected sample; thus we considered all groups from that catalogue with $3 \times 10^{14} < M/M_\odot < 6 \times 10^{14}$. Our default definition of the mass, radius and velocity dispersion come from Eke et al. (2004a), where these quantities are related by

$$M_{\text{dyn}} = \frac{5}{G} R_{\text{rms}} \sigma^2. \quad (1)$$

We excluded a few groups from this selection with large uncertainties on the dynamical mass, due to poor membership or clearly non-Gaussian velocity dispersions. All selected groups have redshifts for at least 15 members.

The velocity dispersions are computed using the gapper estimate of Beers et al. (1990), and R_{rms} is the weighted *rms* projected separation from the cluster centre of all members. The factor of 5 was chosen to give a mass which is in good agreement with dark

Id	Name	RA	Dec (J2000)	Redshift	NIR source	Image size (arcmin)
1	A2734	2.83863	-28.80177	0.061	AAT	21.7 × 21.7
2	A3880	336.97528	-30.57532	0.058	AAT	21.7 × 21.6
3	A3094	47.90881	-26.85087	0.068	2MASS	39.0 × 55.5
4	A1650	194.69207	-1.80407	0.084	CFHT	27.4 × 27.4
5	RBS317	36.294	-29.486	0.060	AAT	21.7 × 21.7
6	MS1306.7-0121	197.31057	-1.61012	0.086	CTIO	31.8 × 31.8
7	S0041	6.38084	-33.04638	0.050	2MASS	38.8 × 65.5
8	A954	153.43704	-0.12043	0.095	CFHT	27.3 × 27.4
9	A1663	195.60600	-2.52938	0.083	2MASS	39.6 × 65.4
10	Chan4990	198.03166	-0.98243	0.084	CFHT	27.3 × 27.4
11	XMM5	48.80986	-29.14884	0.068	2MASS	38.6 × 55.5
12	Chan4991	170.80439	1.08753	0.074	CTIO	31.7 × 31.9
13	XMM3	8.96560	-27.52812	0.071	2MASS	38.8 × 55.4
14	XMM9	201.76353	1.31428	0.081	CFHT	27.3 × 27.4
15	XMM4	199.83071	-0.88001	0.084	2MASS	30.0 × 30.0
16		150.93404	-2.17231	0.096	CTIO	31.8 × 31.9
17	XMM10	202.61707	1.35255	0.082	2MASS	47.1 × 52.0
18		349.50853	-28.17449	0.077	AAT	21.6 × 21.7

Table 1. Basic coordinates of all clusters in our sample, including the source of the infrared imaging used in this paper.

Id	σ (km/s)	M_{dyn} ($10^{14} M_{\odot}$)	R_{rms} (Mpc)	M_{200} ($10^{14} M_{\odot}$)	R_{200} (Mpc)	M_{500} ($10^{14} M_{\odot}$)	R_{500} (Mpc)	r_{max} (R_{500})
1	590±54	3.6±0.8	0.89±0.04	3.25±0.82	1.34±0.12	7.06±2.27	1.32±0.14	0.64
2	580±58	4.8±1.0	1.23±0.04	3.10±0.69	1.32±0.13	3.09±1.17	1.00±0.12	0.80
3	700±53	5.0±1.0	0.88±0.04	5.37±1.25	1.57±0.12	1.49±0.42	0.78±0.07	1.4
4	600±54	5.6±1.2	1.34±0.04	3.31±0.81	1.32±0.12	6.94±0.17	1.30±0.01	0.71
5	550±64	3.5±1.0	1.00±0.04	2.63±0.91	1.25±0.15	1.24±0.10	0.74±0.02	0.80
6	540±69	3.8±1.2	1.12±0.07	2.40±0.82	1.18±0.15	1.40±0.09	0.76±0.02	0.81
7	580±49	4.1±0.9	1.05±0.04	3.13±0.81	1.33±0.11	6.04±3.37	1.21±0.27	0.26
8	680±72	4.5±1.1	0.84±0.06	4.74±1.26	1.47±0.16	1.00±0.14	0.68±0.03	0.70
9	620±63	5.0±1.1	1.12±0.04	3.65±0.96	1.36±0.14	1.68±0.02	0.81±0.00	0.94
10	530±70	3.1±0.9	0.95±0.05	2.28±0.72	1.16±0.15	2.12±0.88	0.87±0.12	1.1
11*	570±59	3.3±0.8	0.87±0.05	2.90±0.85	1.28±0.13	< 0.18	< 0.38	
120	560±57	3.4±0.8	0.93±0.04	2.73±0.77	1.24±0.13	0.91±0.45	0.66±0.10	0.66
13*	640±59	3.6±1.1	0.76±0.08	4.08±1.27	1.43±0.13	< 0.18	< 0.38	
14	720±61	5.5±1.2	0.91±0.06	5.74±1.32	1.59±0.13	0.55±0.07	0.56±0.02	0.80
15	700±69	5.6±1.3	0.98±0.05	5.25±1.39	1.53±0.15	0.74±0.37	0.61±0.08	0.54
16*	480±111	3.2±1.3	1.19±0.09	1.66±0.77	1.04±0.24	< 0.18	< 0.38	
17*	730±97	4.3±1.7	0.69±0.09	5.97±2.59	1.60±0.21	< 0.18	< 0.38	
18*	710±94	5.2±2.1	0.89±0.07	5.53±2.59	1.57±0.21	< 0.18	< 0.38	

Table 2. Dynamical properties, mass and radii measurements for each cluster used in this paper. The radii R_{rms} and R_{200} , with their associated mass estimates M_{dyn} and M_{200} are computed from the galaxy redshifts and positions as described in the text. M_{500} and R_{500} are measured from the X-ray images, and r_{max} is the radius within which X-ray emission is detected, in units of r_{500} . The starred entries are undetected in X-ray, and for these systems we calculate upper limits on R_{500} and M_{500} by extrapolating the correlation between these quantities and L_{bol} . Groups 16 and 18 do not have *Chandra* or *XMM* observations.

matter haloes identified in numerical simulations, using a friends-of-friends algorithm with linking parameter $b = 0.2$. Therefore the mass M_{dyn} corresponds to the mass on scales larger than R_{rms} . We recalculate uncertainties on σ and R_{rms} using a jackknife technique. Uncertainties on σ are typically 10–20 per cent, while those on the radius are typically 5–10%. These lead to dynamical mass estimates which are uncertain by 20–40%.

For comparison with the literature it will also be useful to define a dynamical estimate of the “virial radius”, R_{200} . Following Ramella et al. (2004) we define

$$R_{200} = \frac{\sqrt{3}\sigma}{10H_0(1+z)^{-3/2}} \quad (2)$$

and

$$M_{200} = \frac{3}{G} R_{200} \sigma^2. \quad (3)$$

In contrast with M_{dyn} , this mass depends only on the measured velocity dispersion, and is approximately independent of the radial extent of the friends-of-friends group, since in general σ is a weak function of radius outside the core.

The original 2dFGRS imposed a bright magnitude limit on the spectroscopic selection (Colless et al. 2001). As a result, the brightest galaxies in several of our clusters do not have a redshift from the original survey. Many of these were found in the NASA Extragalactic Database and in the 6dFGRS survey (Jones et al. 2009). In three clusters (8, 10, 11) there are still fairly bright galaxies without

redshifts, but they are subdominant and it makes little difference whether we include them as cluster members or not (we do). For cluster 13, the central very bright galaxy has no redshift available, and this contributes substantially to the cluster luminosity. As it is centrally located we feel confident that it is a cluster member, and thus throughout the paper we assume this is the case.

2.2 X-ray Observations

The description of the acquisition, reduction and analysis of X-ray data from *Chandra* and *XMM* are given in Paper II. Here we summarize the salient details. *Chandra* data have been analyzed using CIAO v4.0 and CALDB v3.4.3, and the standard tools. *XMM* data have been analyzed using the procedure described in Bourdin & Mazzotta (2008). For each cluster we extract the surface brightness and temperature profiles which are then used to estimate the gas and total mass profile following the approach proposed by Vikhlinin et al. (2006). This procedure, which assumes hydrostatic equilibrium and spherical symmetry, involves modeling the 3-D density and 3-D temperature profiles and fitting the projected quantities to the corresponding data set. In the projection we take into account the instrument responses and the effect of the “spectroscopic-like” temperatures (Mazzotta et al. 2004). The radius and mass at an overdensity of 500, R_{500} and M_{500} respectively, are calculated directly from the estimated cluster total mass profile, and are listed in Table 2. Note that because our clusters are nearby, low surface brightness systems, most of the X-ray data do not extend to R_{500} ; in Table 2 we list the maximum radius to which X-ray emission is detected, in units of R_{500} . For most clusters, this is $\gtrsim 70$ per cent; but clusters 7 and 15 require significant extrapolation to obtain M_{500} . The other estimates of mass and radius are included in this table, as well.

Five of the clusters are undetected in X-rays and, for these, we estimate an upper limit to the bolometric X-ray luminosity of about $L_{X,\text{bol}} < 3 \times 10^{42} \text{ ergs s}^{-1}$; although the precise limit depends on the unknown system temperature and metallicity, this limit is appropriate if $kT > 0.2 \text{ keV}$ (Paper II). This is a conservative limit, corresponding to 1000 counts within the field of view. If the clusters were twice as large as this field, we would still expect ~ 250 counts; this would be measurable, even in the *ROSAT* data which is all that exists for groups 16 and 18. We will therefore adopt this upper limit throughout the paper. Corresponding upper limits on R_{500} , M_{500} and M_{gas} are derived by fitting a logarithmic relation between these quantities and L_{bol} , for the 13 detected systems, and extrapolating to the upper limit on luminosity. This yields $R_{500} < 0.4 \text{ Mpc}$, $M_{500} < 1.8 \times 10^{13} M_{\odot}$, and $M_{\text{gas}} < 1.3 \times 10^{12} M_{\odot}$. However, note that these “limits” on mass and radius assume that the undetected clusters lie on the same scaling relations as brighter clusters; if they are in fact relatively deficient in X-ray gas this is unlikely to be the case.

The X-ray image of group 15 shows a clear elongation to the north, and is likely a double system. This is a very low surface brightness system, from which it is difficult to extract a reliable mass profile and hence to estimate R_{500} . The luminosity and temperature used here correspond only to the main part of the cluster, excluding the northern elongation. We have applied the Anderson-Darling test, as described in Hou et al. (2009) to all groups, to test for non-Gaussianity in the velocity distribution. This group is the only one that fails the test, with a 99.7 per cent confident detection of non-Gaussianity. The spatial distribution of the galaxies is extended in the same direction as the X-rays, but this elongation is not clearly correlated with the velocity offsets. Thus, in the near-

infrared data we will not attempt to separate the substructure component.

2.3 Near-infrared data

Of the 18 clusters in our sample, good-quality near-infrared imaging was obtained for 11, over a period of several years at CTIO, AAT and CFHT. For the remaining clusters, the only NIR data available is from 2MASS. Table 1 lists the basic properties of our clusters and gives the telescope and image size of the NIR observations. For the 2MASS clusters, the image size just refers to the area used for our analysis — of course the imaging is all-sky.

2.3.1 CTIO

Near-infrared data were obtained with the ISPI instrument on CTIO, during the nights of May 8-10, 2004. Seeing was $\sim 1''$ in K and two of the nights were fairly cloudy; none were photometric. The instrument has a 10.25×10.25 arcmin field of view, with 0.3 arcsec pixels. A 3×3 mosaic spanning ~ 30 arcmin was obtained for eight clusters, but only six were of good enough quality to include in the present analysis. Data were reduced in IRAF using the CIRRED package, following the reduction algorithm described by Andreon et al. (2000), including bias subtraction, flat fielding and sky subtraction. The data were calibrated by comparing the brightest galaxies with 2MASS, typically involving a few objects per field, resulting in a zeropoint accuracy of about ± 0.2 . The mosaic was combined with the Terapix software SWARP.

2.3.2 AAT

In the fall semester of 2004 we obtained data with the IRIS2 (Tinney et al. 2004) instrument on the AAT. The field of view of this camera is $7.7' \times 7.7'$ with 0.4486'' pixels. Six clusters were observed, by default with a 3×3 mosaic, with a resulting coverage of $23'$. We exclude XMM5 from this analysis, for which only the central position was observed. Cluster 18 was observed in poor conditions and several of the pointings were repeated. The final mosaic was made with only the best images at each position.

The data were reduced following the same standard procedures as for the ISPI data above, but using STARLINK software. The astrometric calibration was done using the very helpful ASTROMETRY.NET software (Lang et al. 2010; Hogg et al. 2008), and the mosaics were combined with SWARP. Photometric calibration was done by comparison of bright galaxies with 2MASS, with similar accuracy to our ISPI data.

2.3.3 CFHT

Four clusters were observed with WIRCAM on the CFHT during the 06A semester. This is a much larger instrument and each cluster was observed with a single pointing, covering a 20 arcmin field with 0.3 arcsec pixels. Data were reduced by Terapix in Aug 2008. The photometric calibration is done by comparison with 2MASS; given the larger field the zeropoint is more precise in these fields than in our ISPI and IRIS2 data, typically better than ~ 0.1 mag *rms*.

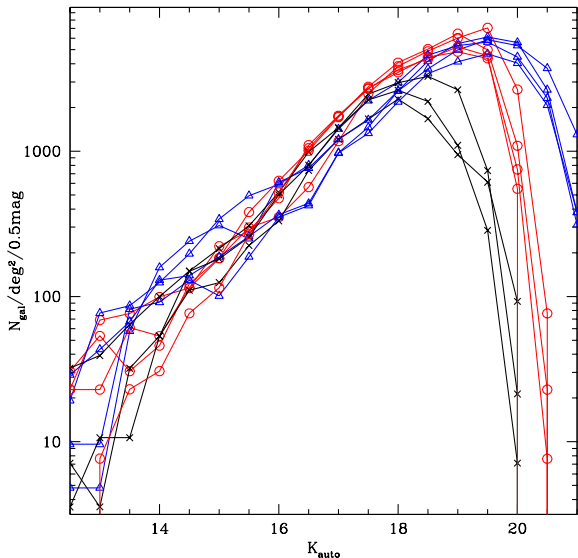


Figure 1. The number of galaxies per square degree and per 0.5 magnitude bin is shown for each of the 11 clusters with deep NIR observations. The black lines and crosses correspond to the CTIO data; red lines and circles represent the AAT data; and the blue lines and triangles represent CFHT data.

2.3.4 2MASS

For the remaining seven clusters in our sample, we do not have deep NIR imaging so we use the public 2MASS catalogues. These however are much shallower than our data, with a limiting magnitude of $K < 13.7$. It is known that the limiting surface brightness of these data is particularly problematic, and the flux from the brightest cD galaxies may be significantly underestimated (e.g. Kochanek et al. 2001; Lin & Mohr 2004). We make no explicit correction for this, and simply note that the total luminosities for these clusters may be underestimated.

3 ANALYSIS

In this section we discuss the data analysis from the eleven clusters observed at CTIO, AAT or CFHT. Fluxes were measured from the reduced data using SExtractor v2.5.0 (Bertin & Arnouts 1996). We use MAG_AUTO as the best estimate of the total magnitude. However, star-galaxy separation is done by comparing $4''$ aperture magnitudes with the Kron radius. The stellar locus is easily identified, separately for each image, and we use this rather than CLASS_STAR. This is only relevant for our analysis when calculating the weights to correct for the spectroscopic sampling rate, discussed below.

We show the number of galaxies per square degree in each cluster in Figure 1. The turnover in the counts gives an indication of the depth of the observations. The CTIO data are generally shallowest, with a limit of $K \sim 18.0$, while the CFHT data are deepest.

Our NIR photometry is matched to the original 2dF imaging catalogues, by searching for the closest match within a $3''$ aperture. The 2dF catalogues are blue-selected, with $b_J < 19$, and this limits our sample size. We show a colour-magnitude diagram of our data in Figure 2, restricted to galaxies within 1500 km/s of each cluster. The red sequence of galaxies typical of dense environments is

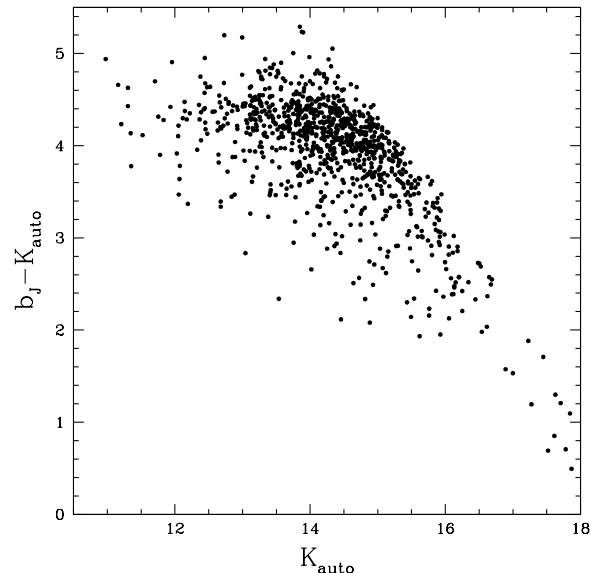


Figure 2. The colour-magnitude relation for observed galaxies with redshifts within 1500 km/s of each cluster. Redshifts from the 2dFGRS were obtained only for galaxies with $b_J < 19$; thus our sample becomes incomplete for red galaxies with $K > 14.5$.

evident, and the blue selection means our sample becomes incomplete for $K > 14.5$. This is ~ 3 magnitudes brighter than our K detection limit, so there is no additional incompleteness in the NIR imaging.

Brighter than $K = 14.5$ we calculate a K -dependent sampling completeness for each cluster, as shown in Figure 3. This is the ratio of the number of galaxies with a redshift to the total number detected in the NIR, considering only galaxies within 600kpc of each cluster centre. In general, the completeness is close to 80 per cent over most of the magnitude range we're interested in, falling to 50 per cent at $K = 14.5$. We weight all galaxies by the inverse of this number for all subsequent analysis. In practice the weight is calculated separately for each cluster based on a smooth fit to the completeness function in the relevant field.

We use the mean redshift of each cluster to calculate absolute magnitudes for all members, using a cosmology of $\Omega_m = 0.3$, $\Omega_\Lambda = 0.7$, and $h = 0.7$. The most distant cluster in our sample is at $z = 0.096$, which corresponds to a luminosity distance of 442.0 Mpc. We correct for Galactic extinction using the Schlegel et al. (1998) dust maps (though this is entirely negligible), and apply a k -correction of $k(z) = -6 \log(1+z)$, following Kochanek et al. (2001). For our most distant cluster, therefore, we are complete in luminosity for $M_K < -23.5$.

First, we present the cumulative luminosity function from the combination of all eleven clusters with follow-up NIR data. We include all galaxies with redshifts within 1500 km/s of the cluster redshift, and within a distance R_{rms} from the centre¹. We show the weighted number of galaxies brighter than a given M_k absolute magnitude, per cluster in Figure 4. Plotted for comparison are Schechter functions with $M_K^* = -24.3$ (Balogh et al. 2001a) and $\alpha = -0.5$ (solid) or $\alpha = -1.0$ (dashed). These are not fit to the data, but are meant only to guide the eye. The presence of central

¹ For clusters 1, 2, and 5 the maximum radial coverage is defined by the extent of the IRIS2 imaging.

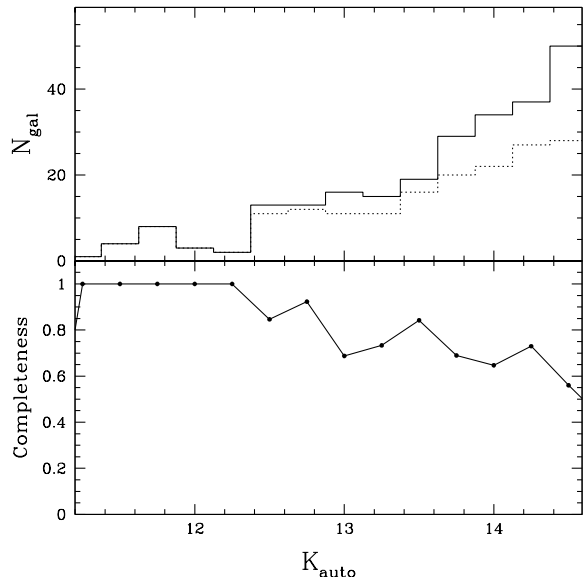


Figure 3. Top panel: The solid line shows the K magnitude distribution of all detected galaxies in our images, while the dotted line shows the distribution of galaxies with redshifts from the 2dFGRS. Bottom panel: The connected points represent the sampling fraction, which is the fraction of K -detected galaxies with redshift, as a function of magnitude. Shown here is the average selection function; in practice we compute this separately for each cluster. Only galaxies within 600 kpc of the cluster centre are included.

bright galaxies in most of our clusters leads to an excess relative to the Schechter function, at the bright end, as is seen in more massive clusters (e.g. Popesso et al. 2005b). Recall that, for $M_K > -23.5$ our sample is incomplete, and this limit is indicated by the dotted line.

4 RESULTS

We now proceed to calculate the total K luminosity of each cluster, L_K . We simply sum the luminosity of all galaxies within 1500 km/s and R_{rms} of the cluster centre, brighter than the $K = 14.5$ limit. To correct for galaxies below this limit we model the luminosity function as a Schechter function with $M_K^* = -24.3$ and $\alpha = -1.0$. As our data reach at least 0.6 mag fainter than M_K^* for all clusters, this correction is always less than 20%.

We also include the seven clusters without deeper NIR data in our analysis; these are shown as open symbols on the following Figures. For these clusters, the 2MASS limiting magnitude is much brighter, $K < 13.7$, and for three of them the corresponding correction for fainter galaxies is larger than a factor of two.

We do not attempt to measure or correct for intracluster light. This remains an important uncertainty in all such work, with some claims that a large fraction of the stars in galaxy groups are found in this component (Gonzalez et al. 2005; McGee & Balogh 2010). For clusters in the mass range of our sample, however, we expect the intracluster light contribution to be less than about 20 per cent (e.g. Zibetti et al. 2005).

The statistical uncertainty on L_K is dominated by the statistical uncertainty on R_{rms} , since that quantity determines the radius

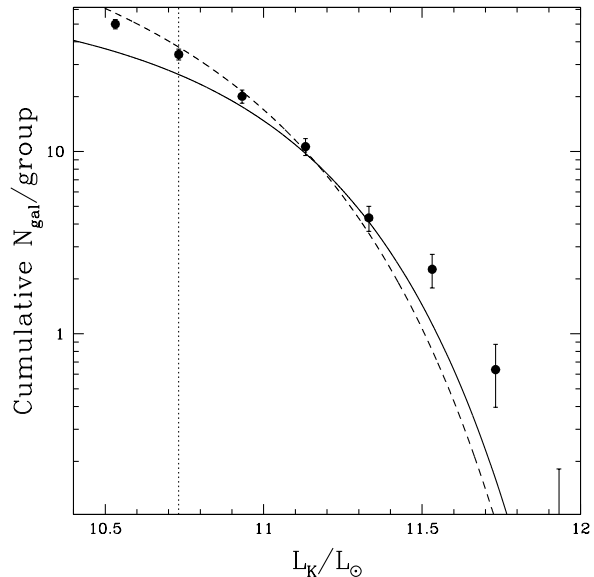


Figure 4. The cumulative luminosity function for our eleven clusters with deep NIR imaging. This includes only galaxies within 1500km/s of the cluster redshift, and within R_{rms} of the centre. The dotted line indicates the luminosity limit corresponding to $M_K > -23.5$; at luminosities fainter than this our sample is incomplete due to the blue selection of the 2dFGRS. Two Schechter functions are shown to guide the eye; they are not fit to the data. Both have $M_K^* = -24.3$, taken from (Balogh et al. 2001a). The solid line has a shallow faint-end slope of $\alpha = -0.5$, while the dashed line shows $\alpha = -1.0$.

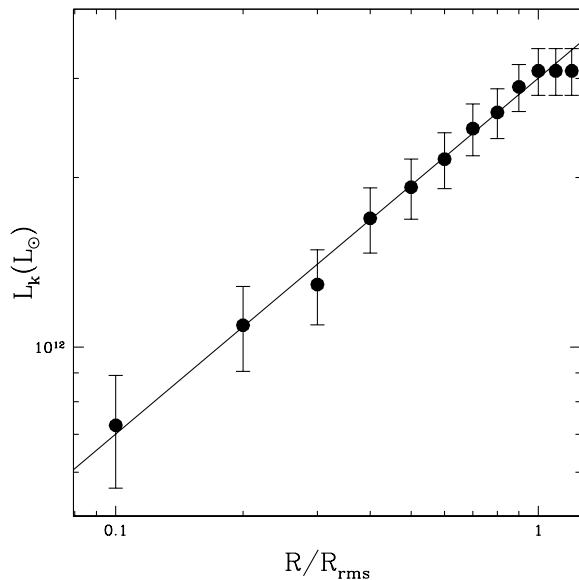


Figure 5. The cumulative K -band luminosity of our clusters, as a function of distance from the centre. This excludes clusters with only 2MASS photometry, or for which our NIR coverage does not extend to R_{rms} . Error bars show estimated 1σ uncertainties arising from Poisson fluctuations in the number of galaxies contributing to each bin. The solid line is a fit to the data with $R/R_{\text{rms}} < 1.0$, and has a slope of 0.63. This relation is used to calculate how the uncertainty on L_K depends on our uncertainty on R_{rms} , and to correct the total luminosity of clusters for which our NIR coverage does not extend to the radius of interest.

Id	N ($r < R_{\text{rms}}$)	$L_K(r < R_{\text{rms}})$ ($10^{12} L_{\odot}$)	N ($r < R_{200}$)	$L_K(r < R_{200})$ ($10^{12} L_{\odot}$)	N ($r < R_{500}$)	$L_K(r < R_{500})$ ($10^{12} L_{\odot}$)
1	28	3.12 ± 0.12	29	4.10 ± 0.12	29	4.07 ± 0.12
2	31	4.48 ± 0.10	31	4.69 ± 0.10	31	3.93 ± 0.10
3	15	2.84 ± 0.08	31	5.37 ± 0.15	11	2.25 ± 0.06
4	40	8.01 ± 0.23	39	7.39 ± 0.21	37	6.99 ± 0.20
5	23	3.33 ± 0.11	23	3.84 ± 0.11	21	2.43 ± 0.10
6	18	2.34 ± 0.14	18	2.34 ± 0.14	14	1.94 ± 0.12
7	27	3.95 ± 0.13	28	4.49 ± 0.13	27	3.95 ± 0.13
8	15	4.11 ± 0.20	20	5.03 ± 0.25	14	3.95 ± 0.19
9	17	5.61 ± 0.15	24	8.07 ± 0.22	7	1.95 ± 0.05
10	20	3.13 ± 0.13	25	3.69 ± 0.15	17	2.65 ± 0.11
11	14	3.22 ± 0.11	22	5.64 ± 0.19	5	1.09 ± 0.04
12	24	3.86 ± 0.11	31	4.84 ± 0.14	16	2.70 ± 0.08
13	3	0.64 ± 0.04	6	1.24 ± 0.08	2	0.47 ± 0.03
14	14	1.64 ± 0.08	21	2.85 ± 0.11	9	1.22 ± 0.06
15	13	5.05 ± 0.17	21	8.85 ± 0.30	9	3.71 ± 0.13
16	13	2.45 ± 0.17	10	1.98 ± 0.14	3	0.97 ± 0.07
17	4	2.52 ± 0.18	6	3.75 ± 0.26	3	1.96 ± 0.14
18	4	0.89 ± 0.05	5	1.33 ± 0.06	2	0.66 ± 0.04

Table 3. Derived properties of the stellar population for all clusters in our sample. Throughout the paper, stellar masses are calculated using a universal mass-to-light ratio in the K -band, $\gamma = 0.7$.

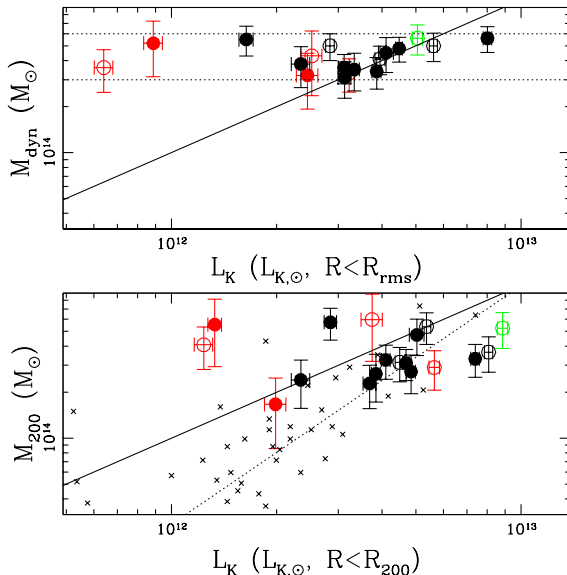


Figure 6. *Top panel:* The dynamical mass of our clusters is shown as a function of their total K luminosity, integrated out to R_{rms} . The horizontal, *dashed lines* indicate the selection limits imposed on the sample, while the *solid line* represents $M_{\text{dyn}}/L_K = 100$. Open circles represent clusters with only 2MASS imaging. The *green point* corresponds to the group 15, an outlier on the $L_K - L_X$ relation that will be identified on Figure 7, while the *red points* are undetected in X-rays. *Bottom panel:* The same, but for M_{200} and the K luminosity within R_{200} , where these quantities are measured from the velocity dispersion alone, following Ramella et al. (2004), whose data are shown as the crosses without error bars. The *solid line* represents $M_{200}/L_K = 100$, while the *dotted line* represents $L_K \propto M^{0.64}$ as found by Ramella et al. (2004).

within which the luminosity is integrated². In Figure 5 we show

² Poisson-type uncertainties on the number of cluster members N are not really appropriate in this context, as for a specific cluster N is a fixed num-

ber without uncertainty. Statistical uncertainties on the photometry, while of order 5%, are negligible because they are reduced by \sqrt{N} when applied to the total luminosity.

the cumulative luminosity as a function of r/R_{rms} , only including clusters observed out to R_{rms} , with AAT, CTIO or CFHT. The best-fit line to the data where $R/R_{\text{rms}} < 1$ has a slope of 0.63. Thus, the statistical uncertainty on L_K is only $\sim 0.63\Delta R/R_{\text{rms}}$ which, given the typical 10 per cent uncertainty on R_{rms} , corresponds to a ~ 6 per cent uncertainty on L_K . In contrast, the typical uncertainty on M_{200} is 20–40 per cent, as it is proportional to σ^3 (see § 2). We use this relation for $L_K(R)$ to correct the total luminosity of those clusters for which NIR coverage only extends out to $r < R_{\text{rms}}$.

4.1 Correlation between stellar luminosity and dynamical mass

The total K luminosity of each cluster, integrated to either R_{rms} , R_{200} or R_{500} , is given in Table 3. We also show the total number of galaxies with redshifts and NIR data within each radius.

We have shown above that L_K can easily be measured with a precision about five times better than that of M_{dyn} , a point that has been noted by others (e.g. Popesso et al. 2005a). This makes it a very useful indicator of system mass, although of course it is tracking a fundamentally different quantity than M_{dyn} . In the top panel of Figure 6 we show the correlation between these two quantities. The clusters were selected to span a factor of only three in M_{dyn} , but they show a factor ~ 10 spread in L_K . Note that the apparent lack of correlation is likely a consequence of limited dynamic range in M_{dyn} , together with significant scatter between M_{dyn} and L_K . Most of the clusters are consistent with $M_{\text{dyn}}/L_K = 100$, shown as the solid line. The green and red points indicate X-ray underluminous systems, which will be discussed below. Note these most of these have M_{dyn}/L_K ratios in good agreement with the rest of the sample.

To compare with data from Ramella et al. (2004) we compute R_{200} and M_{200} in precisely the same way they do, using equations 2 and 3. We measure L_K also within R_{200} , and show the

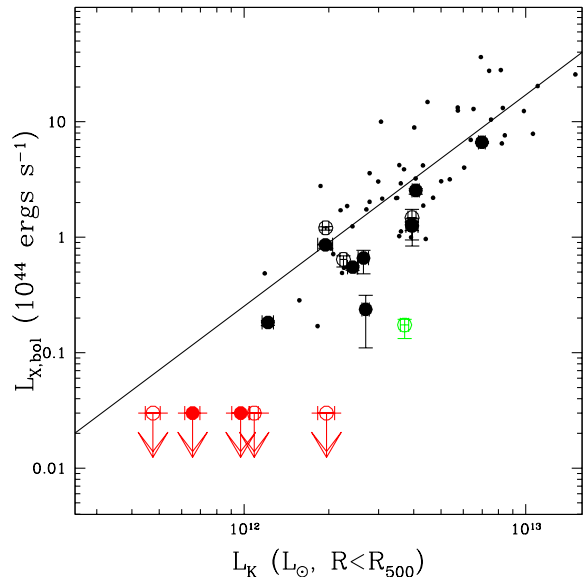


Figure 7. The bolometric X-ray luminosity of our clusters are compared with L_K ; both quantities are computed within R_{500} as determined from the X-rays. The small, filled circles are the clusters of Lin & Mohr (2004), with X-ray luminosities taken from Reiprich & Böhringer (2002), and the solid line is a linear fit to these data. The X-ray undetected clusters (red points) are represented as upper limits, with L_K measured within $R_{500} \sim 0.4$ Mpc. The cluster marked in green is detected in X-ray, but is a clear outlier on this plot, with about five times more near-infrared luminosity than expected.

correlation with M_{200} in the bottom panel of Figure 6. The data of Ramella et al. (2004) are shown as the small crosses. The solid line represents a mass-to-light ratio of $M_{200}/L_K(r < R_{200}) = 100$, while the dotted line shows the relation found by Ramella et al. (2004), $L_K \propto M^{0.64}$. Most of the clusters are consistent with the data of Ramella et al. (2004), though there are clear outliers. Most notable are the two groups (13 and 18) that have stellar masses well below that expected from their dynamical mass. The fact that they are undetected in X-rays suggests that their dynamical mass is significantly overestimated; however, we will show (Fig 7) that the lack of X-ray emission is still surprising given their total stellar mass.

4.2 X-ray properties

In Figure 7 we show the bolometric X-ray luminosity of each cluster as a function of its total K -band luminosity. Both quantities are computed within R_{500} as determined from the X-ray emission (Paper II). Throughout the paper, both the bolometric luminosity L_X and X-ray temperature include contribution from any cool-core. This maximizes the scatter and allows us to test for any correlation between cool-core emission and optical properties of the clusters. We compare our measurements with the data of Lin & Mohr (2004), with X-ray luminosities (also uncorrected for cool cores) obtained from Reiprich & Böhringer (2002); the solid line represents a least-squares fit to these data. There is considerable scatter among our clusters, but most of the X-ray detected clusters are consistent with those of Reiprich & Böhringer (2002). There is some indication that our clusters lie toward the lower edge of the distribution. This is likely due to the well-known Malmquist bias that

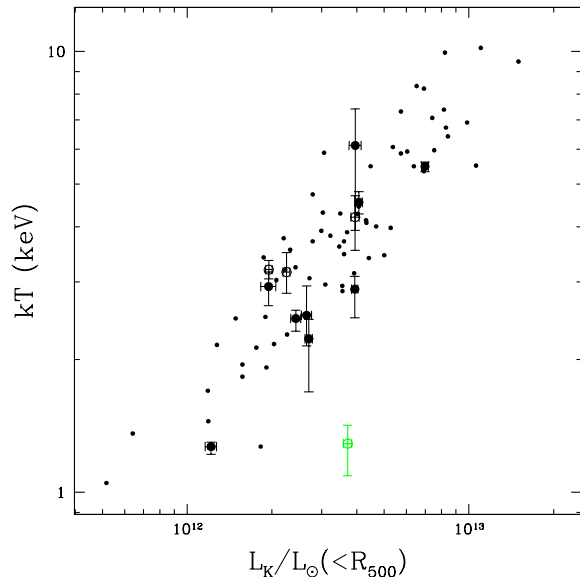


Figure 8. The X-ray temperature of our 13 detected clusters are compared with L_K as measured within R_{500} . The small, filled circles are the clusters of Lin & Mohr (2004), with X-ray temperatures taken from Horner (2001). The green symbol corresponds to group 15, which is also an outlier in figure 7.

affects X-ray selected samples (e.g. Ikebe et al. 2002; Pratt et al. 2009; Vikhlinin et al. 2009; Rykoff et al. 2008b). We therefore expect our dynamically-selected cluster sample to have a representative distribution of L_X .

One of the systems (group 15, in green) appears to have significantly low L_X for its stellar luminosity. Recall from § 2.2 that group 15 shows substructure in the X-ray and a significantly non-Gaussian velocity distribution. The luminosity and temperature used here correspond only to the dominant component. Treating the whole system as one results in a temperature increase of ~ 10 per cent, and a L_X increase of $\sim 73\%$. This does not change the status of this system as an outlier on this plot.

The limits on the five undetected clusters imply that they are underluminous in X-ray by up to a factor of 10. Recall that, for these clusters the radius R_{500} is based on the radius expected for a cluster at our L_{bol} detection limit. If the clusters are actually deficient in X-ray emitting gas, the true value of R_{500} , and hence L_K , could be larger. This would make the discrepancy worse, since the limit on L_X is based on a fixed number of counts in the field of view.

The total X-ray luminosity is known to be a relatively poor tracer of mass, but a good tracer of the thermodynamic history of the gas (e.g. Balogh et al. 2006). The X-ray temperature, while more difficult to measure, is a much better representation of the size of the potential. Thus, in Figure 8 we show the correlation between temperature and L_K for the 13 clusters in our sample with X-ray detections. The temperature measurements are described in Paper II. Again, these data are compared with data from Lin & Mohr (2004), with temperatures (uncorrected for cool cores) from Horner (2001). Our data generally agree very well with the relation defined by the Lin & Mohr (2004) data, confirming that L_K is a good tracer of cluster mass. Interestingly, the detected cluster 15 (in green), that is a significant outlier on the $L_K - L_X$ relation, also lies off the $L_K - T$ relation in Figure 8. This could indicate that it is a high

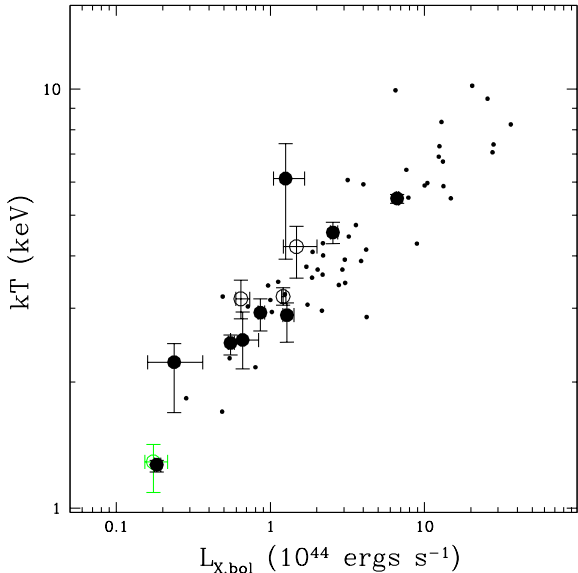


Figure 9. The correlation between X-ray luminosity and temperature for the 13 detected clusters, compared with the Lin & Mohr (2004) cluster sample. The green point indicates group 15, an outlier on the $L_K - L_X$ relation. The fact that it appears consistent with the rest of the data shown here suggests that the offset is due to unusually high L_K .

stellar content, rather than low X-ray luminosity, that makes it unusual. This is also seen in the $L_X - T$ relation, shown in Figure 9, where our data are compared with those of Horner (2001). Group 15 appears consistent with this relation. We again note, however, the possible, small offset of the whole sample toward lower L_X relative to Lin & Mohr (2004), indicative of Malmquist bias in X-ray flux-limited samples (Paper II).

4.3 Stellar mass

Finally, we convert the K -luminosity into a stellar mass, assuming a stellar mass-to-light ratio $\gamma = 0.7M_\odot/L_\odot$ (Lin & Mohr 2004). In Figure 10 we compare this with the gas mass within R_{500} , as measured from the X-ray observations. The lines represent different values of the baryon fraction found in stars, $f = M_{\text{star}}/(M_{\text{star}} + M_{\text{gas}})$, of 0.075, 0.12 and 0.2. Our data show considerable scatter, but on average our detected clusters are consistent with ~ 12 per cent of their baryons in stars (neglecting intracluster light), as typically found for more massive clusters (e.g. Balogh et al. 2001b). For the five undetected clusters, we show the estimated upper limit of $M_{\text{gas}} < 1.3 \times 10^{13} M_\odot$, and compute the stellar mass within the radius $R_{500} \sim 0.4$ Mpc that would be consistent with an otherwise normal cluster at our X-ray detection limit. These limits imply that > 20 per cent of the expected baryons are in the form of stars. If R_{500} is larger than we have estimated, for example if their dynamical masses are correct, then M_{star} could be substantially larger. Thus, our limit on the stellar fraction here is robust. These are clearly very different systems from the rest of the sample, with little or no associated X-ray emitting gas.

We next compare the stellar mass with the total mass M_{500} , as estimated from either the X-ray mass profiles (Figure 11), or the galaxy dynamics (Figure 12). In the latter case, we use $R_{500} = \sqrt{200/500}R_{200}$, and $M_{500} = \sqrt{200/500}M_{200}$. The lines in this figure represent total stellar fractions of $M_{\text{stars}}/M_{500} = 0.005$,

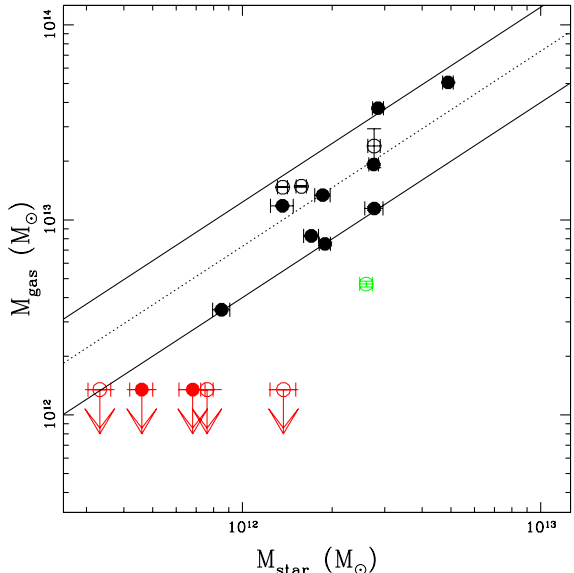


Figure 10. The total gas mass within R_{500} , as measured from the X-ray emission, is compared with the total stellar mass within the same radius, computed from L_K assuming $\gamma = 0.7M_\odot/L_\odot$. Lines represent different values of $f = M_{\text{star}}/(M_{\text{star}} + M_{\text{gas}})$ for comparison. The dotted line shows $f = 0.12$, while the two solid lines show $f = 0.075$ (top line) and $f_{\text{star}} = 0.2$ (bottom). The X-ray undetected clusters are represented as red upper limits, with L_K measured within $R_{500} \sim 0.4$ Mpc. The green symbol represents group 15, the outlier on Figure 7.

0.01 and 0.03. The data are compared with Lin & Mohr (2004) and Gonzalez et al. (2007). For the latter, we exclude the intracluster light component, as neither our data nor that of Lin & Mohr (2004) includes this. We omit the two clusters in the Gonzalez et al. (2007) sample that are strongly affected by line-of-sight projections; the two lowest-mass clusters remaining in their sample have the most uncertain R_{200} and Gonzalez et al. (2007) exclude them for some of their analysis, though we retain them here for the sake of completeness.

In general the agreement with the Lin & Mohr (2004) data is good, but our lowest-mass clusters ($M_{\text{star}} < 4 \times 10^{12} M_\odot$) have systematically lower stellar fractions than similar systems from Gonzalez et al. (2007). In particular, none of the X-ray detected clusters have total stellar fractions greater than about 3 per cent, and most are closer to 1 per cent. Our data are in good agreement with the theoretical prejudice of Balogh et al. (2008), that the stellar fraction in groups and clusters cannot be much larger than observed in the most massive systems.

Some of the five clusters that are undetected in X-rays appear to have unusually high stellar fractions; however recall that the radius R_{500} within which the stellar light is integrated is not directly measured for these systems. In Figure 12 we use dynamical measures of M_{500} and R_{500} , which we can measure uniformly for the whole sample. Here we see that all our clusters are remarkably uniform, with a total stellar fraction close to ~ 1 per cent in most cases.

Finally, we note that, for the most part, the open symbols on Figures 6–10, which indicate the clusters with only 2MASS imaging, do not appear distinct from the other points on the plots. This gives confidence that our results are not significantly biased by the lack of deeper imaging in these systems. The obvious exception is

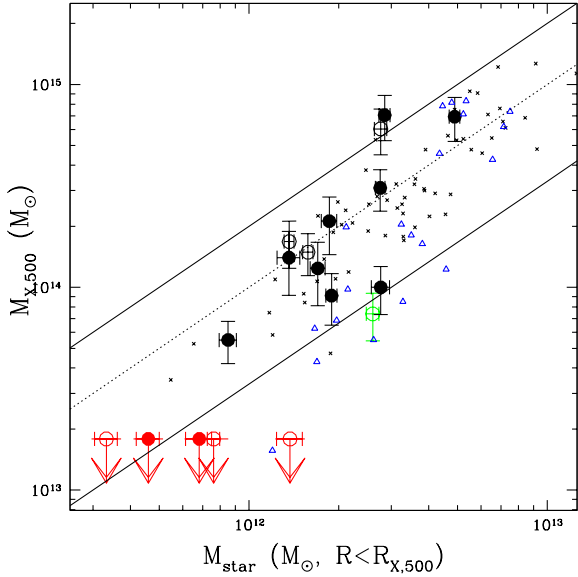


Figure 11. The total cluster mass within R_{500} , as measured from the X-ray emission, is compared with the total stellar mass within the same radius, computed from L_K assuming $\gamma = 0.7M_{\odot}/L_{\odot}$. Lines represent different values of $f = M_{\text{star}}/M_{500}$ for comparison. The dotted line shows $f = 0.01$, while the two solid lines show $f = 0.005$ (top line) and $f_{\text{star}} = 0.03$ (bottom). The X-ray undetected clusters are represented as red points, and the green symbol represents group 15, the outlier on Figure 7. Small crosses are data from Lin & Mohr (2004), and blue triangles are clusters from Gonzalez et al. (2007), excluding the intracluster light component, as presented in Balogh et al. (2008). With the exception of the single outlier, all our detected clusters have total stellar fractions less than 3 per cent, with an average of about 1 per cent. These stellar fractions are consistent with those of Lin & Mohr (2004), but lower than found by Gonzalez et al. (2007) in their lowest-mass systems.

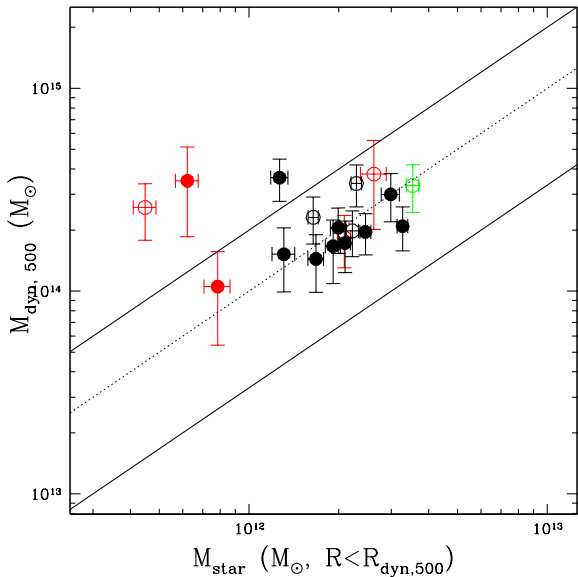


Figure 12. The same as Figure 11, but where R_{500} and M_{500} are now estimated from the galaxy dynamics, for all clusters in our sample.

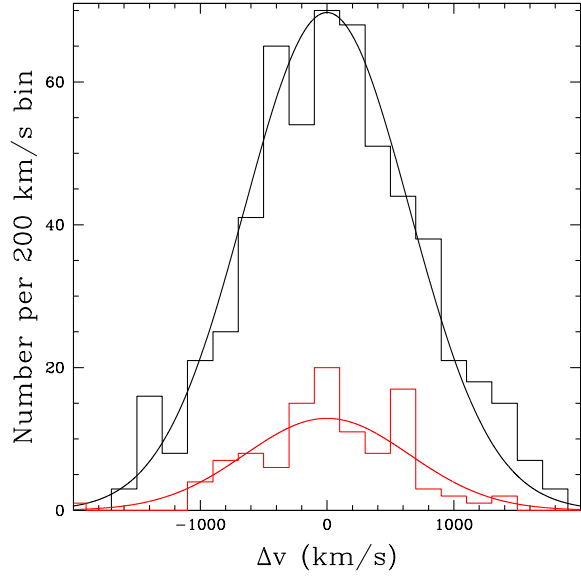


Figure 13. The velocity distribution for our cluster sample, considering galaxies within 1 Mpc of the recomputed centre. The *red* histogram corresponds to the five undetected systems. The rest of the clusters are included in the *black* histogram. The smooth lines are Gaussian functions with $\sigma = 650\text{km/s}$, normalized to match the total number of objects in each histogram.

group 15, which is an outlier on most plots. This, however, may be related to the fact that it is a clear double-system, and the only cluster with a significantly non-Gaussian velocity distribution.

5 DISCUSSION

Of the 18 clusters observed, five are undetected in X-ray, and one (group 15) appears to have an anomalously high stellar content given its X-ray properties. The five non-detections have a stellar mass which is ~ 1 per cent or less of their total dynamical mass, consistent with most other clusters. However, the strong limits on their X-ray luminosity imply that there is little or no associated X-ray emitting gas. For these systems, either their *virialised* mass is $M < M_{\text{dyn}}$, or they are extremely underluminous due to excess heating or cooling.

Of these, the least likely possibility is that all the gas has cooled to form stars. Figure 12 suggests that, if anything, the ratio of stellar mass to dynamical mass in these clusters is *lower* than that of the normal systems. Normal clusters have ~ 7 times more gas mass than stellar mass (Figure 10); if all that gas formed stars we would expect to see stellar luminosities ~ 7 times higher than normal clusters of the same dynamical mass, and this is clearly not the case.

On the other hand it is difficult to rule out the possibility that the gas in the underluminous clusters has been heated or expelled, as predicted by some models (e.g. Bower et al. 2008; McCarthy et al. 2010a). In this case of course there should be some gas present, but at low density and low surface brightness. The only way to definitively distinguish between this and the following scenario is through X-ray observations deep enough to detect either this hot, diffuse gas or the gas associated with individual galaxies.

This leaves the possibility that the undetected clusters are unrelaxed, and have not yet reached virial equilibrium (e.g.

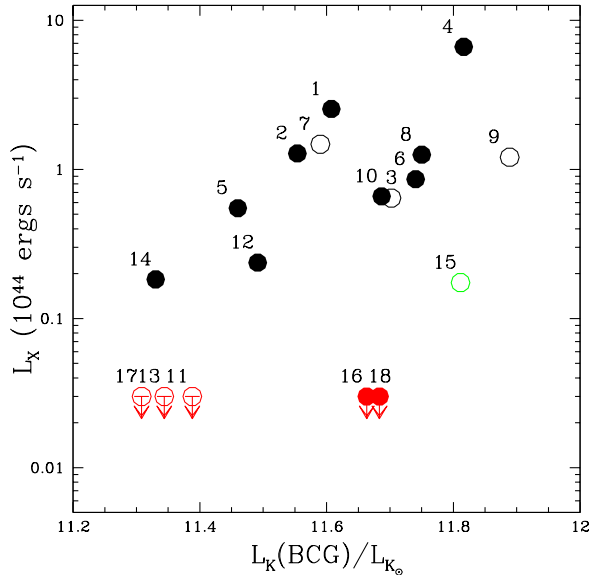


Figure 14. For each cluster, we show the cluster X-ray luminosity as a function of the K -band luminosity of the brightest cluster member (BCG). Point symbols are as in other plots, with the *green* symbol for the outlier group 15, and *red* symbols for undetected clusters. Clusters are numbered according to their entry in Table 1. Open symbols represent clusters for which the near-infrared imaging comes from 2MASS. The lack of correlation here demonstrates that the clusters which are underluminous in X-ray host BCGs that are just as luminous as the rest of the sample.

Popesso et al. 2007; Dietrich et al. 2009; Rasmussen et al. 2006). It is even possible that some of these systems are chance projections, in which case the appropriate “virialised mass” to consider is just that of the dominant galaxy. To shed light on this issue we now investigate this using the spatial and dynamic information available for each cluster. Since these results are somewhat sensitive to the choice of centre and radius, we recompute these quantities for all the following analysis, including galaxies with redshifts from surveys other than the original 2dFGRS. Specifically, we select all galaxies with redshifts, within 1.5 Mpc of the original centre and 1500 km/s of the original cluster redshift. We adopt the central position and redshift as the geometric mean of these quantities, unweighted for selection or luminosity.

In Figure 13 we show the velocity distributions for the “normal” clusters (black line), including only galaxies within 1 Mpc of the recomputed centre. We compare this with the five undetected clusters, as the red line. Overplotted for comparison are Gaussian functions with a velocity dispersion of 650 km/s, for comparison. A Kolmogorov–Smirnov test shows that the velocity distributions of the undetected clusters are consistent with that of the rest of the sample, with a 13 per cent probability of either being drawn from the same parent distribution. Thus, given the limited statistics, we find no evidence for differences in the dynamical state of the underluminous systems. As described in § 2.2, we have also computed the Anderson-Darling statistic, as described by Hou et al. (2009), for each group. Only group 15 shows significant non-Gaussianity in the velocity distribution, at > 95 per cent confidence.

Other indications of a relaxed cluster could be the presence of a dominant galaxy near the X-ray centre (e.g. Dariush et al. 2010), and an approximately spherical, centrally-concentrated galaxy distribution. In many of the clusters, there is an obvious dominant

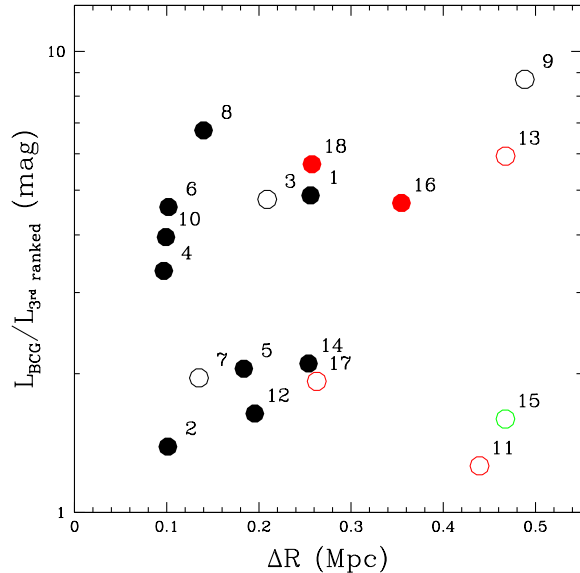


Figure 15. For each cluster, we show the luminosity ratio of the brightest and third-brightest galaxies (in K), as a function of the distance of the brightest galaxy from the recomputed cluster centre. Symbols are as in Figure 14.

galaxy, large and luminous, near the centre of the X-ray image. To quantify this, we have selected all cluster members within 700 km/s of the mean redshift and 500 kpc of the recomputed centre, and identified the most luminous (in K) as the BCG. Figure 14 shows the luminosity of each of these BCGs, as a function of the host cluster L_X . There is little correlation here, although we note that three of the X-ray undetected clusters have BCGs that are among the least luminous in the sample (unfortunately, all three have only shallow 2MASS imaging, and thus the total luminosities may be significantly underestimated). It is also interesting that group 15, which has a high stellar mass given its L_X , has one of the most massive BCGs in the sample.

Next we calculated the luminosity ratio between the first- and third-ranked galaxy, $L_{K,13}$. In Figure 15 we show this as a function of ΔR , which is the distance in Mpc between the brightest cluster galaxy (BCG) and the geometric centre of the cluster, recomputed as above. Interestingly, the distribution of the X-ray undetected clusters (and also the outlier group 15) is distinct from most of the “normal” systems, in the sense that their BCG is at least 250 kpc from the centre. However, we note that, of the 12 otherwise “normal” systems, only about half have a dominant ($L_{K,13} > 3$), centrally located ($\Delta R < 250$ kpc) BCG.

We now attempt to quantify the spatial distribution of the most luminous galaxies, i.e. those that are at most 0.6 mag fainter than M_K^* , so that we are equally deep in all clusters. The undetected cluster 18 only has three galaxies above this limit, so we omit it from the following analysis. We calculate the concentration as the fraction of such cluster members within $0.5R_{\text{rms}}$. For the elongation, we first perform a least-squares regression analysis to find the principle axis of each cluster on the sky; then we calculate the *rms* dispersion perpendicular to and parallel to this axis. The elongation is the ratio of the two values, always defined as the larger divided by the smaller so the ratio is greater than unity. The results are shown in Figure 16, where the points are colour-coded as before. Error bars are computed using a jackknife resampling.

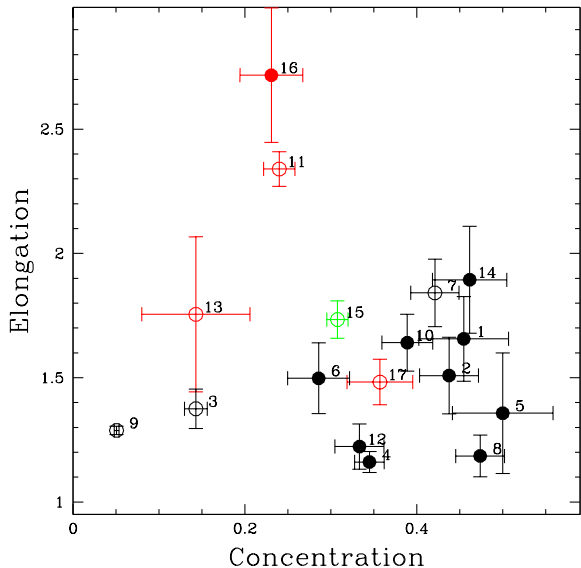


Figure 16. For each cluster (except cluster 18, which has too few members for this analysis), we show its elongation as a function of concentration. Both quantities are computed for a subset of cluster members, brighter than $M_K^* + 0.6$ and with velocities within twice the cluster velocity dispersion. The concentration is the fraction of galaxies that lie within $0.5R_{\text{rms}}$, while the elongation is the ratio of the *rms* values about the directions perpendicular to and parallel to the least-squares fit correlation in spatial coordinates. Symbols are the same as figure 15. Three of the undetected clusters show low values of concentration, and two of these are also highly elongated.

Interestingly, most of the X-ray underluminous systems again appear separated from the majority of the population, as either low-concentration or highly elongated clusters. Only cluster 17 lies in a region of the plane occupied by the majority of normal clusters. Note that cluster 16 is highly elongated; from Figure 15 we see that it has a distinctly dominated galaxy, but located 350 kpc from the centre. This may indicate a merging or otherwise unrelaxed system. Cluster 18, which is the only other X-ray undetected system with a dominant, centrally-located galaxy, has too few members to measure either quantity shown here with adequate precision. Again, however, there are examples of clusters (3 and 9) with normal X-ray properties and equally low concentrations.

This result needs to be approached with some caution, as there are multiple parameters at work here, related to the magnitude and velocity selections, the choice of centre, and the definition of concentration. Nonetheless, we tentatively conclude that it seems likely dynamical age plays some role in the X-ray luminosity of a given cluster. All the clusters that appear relaxed in the optical – with a dominant central galaxy (within 250kpc of the cluster centre, and at least three times brighter than the third-ranked galaxy), a centrally concentrated (> 0.25) galaxy population, and a spatial axis ratio of less than two – show normal X-ray properties³. There is no evidence for excess heating or cooling in these systems. However, this does not mean that X-ray selection returns a sample of relaxed clusters; of the twelve clusters with normal X-ray properties (i.e. excluding the outlier 15 and the undetected clusters), seven show

³ The possible exception is group 18, which has a dominant, near-central galaxy but for which we are unable to measure elongation and concentration.

signs of dynamical youth. In other words, neither optical- nor X-ray selection returns a sample of dynamically relaxed clusters, which is certainly not a surprise. It is worth emphasizing though that any signs of dynamical disturbance are fairly subtle. With the possible exception of group 15, none of our clusters look like strongly merging systems either in the X-ray or optical images, and the velocity distributions (based on few members) do not show obvious signs of nonvirialisation.

Thus, with the present data, we can plausibly argue that the undetected systems might be unvirialised and that this is the origin of the low X-ray emission. On the other hand, the differences between the luminous and under-luminous systems are remarkably subtle and we cannot rule out that the difference is due to a substantial amount of ejected gas, as predicted by some models (e.g. Bower et al. 2008; McCarthy et al. 2010a).

6 CONCLUSIONS

We have presented a sample of 18 clusters selected from Eke et al. (2004a) based on their dynamical mass alone, and followed up sixteen of them with pointed *Chandra* and *XMM* observations. The clusters were selected based on optical properties alone, to lie in a narrow range of dynamical mass $3 \times 10^{14} < M/M_{\odot} < 6 \times 10^{14}$. We summarize our findings as follows:

- Of the 18 clusters studied, five are undetected in X-ray emission. The limits on their X-ray luminosity are significantly below the luminosity that would be expected given their stellar mass. The rest lie within the scatter defined by X-ray selected samples, but toward the low-Lx end of the scatter. This is in good agreement with previous studies by e.g. Bower et al. (1997), Rykoff et al. (2008a), Hicks et al. (2008) and Rasmussen et al. (2006).
- Stars make up less than 3 per cent of the total mass in all of our clusters, with an average of about 1 per cent. The fraction of detectable baryons in the form of stars is about 12 per cent on average, with a range of approximately 7 – 20 per cent, though the clusters that are undetected in X-ray emission have implied fractions of > 20 per cent.
- The undetected clusters have velocity distributions that are not significantly different from the rest of the sample. However, they all either lack a central, dominant galaxy, or show spatial distributions that are of low concentration or high elongation, relative to most of the “normal” clusters. Similar conclusions have been reached by Popesso et al. (2007) and Dietrich et al. (2009).

We conclude that the redshift–selection of low–mass clusters returns a heterogeneous sample. Most of those systems that are detected in X-ray have gas properties that are consistent with X-ray selected samples, though somewhat underluminous on average. The main difference is that a fraction (6/18 in our case) have surprisingly low X-ray luminosity, given their stellar content. It remains an open question, whether this is because such clusters are dynamically young (unvirialised) or because the hot gas has been expelled or rarefied due to energetic processes associated with galaxy formation.

7 ACKNOWLEDGMENTS

We thank the referee for a thorough and helpful report, and Stefano Andreon for pointing out a few errors in the original text. MLB and TL would like to thank David Gilbank and Sean McGee

for many useful discussions about this work and comments on the draft. MLB would like to thank to Patrice Bouchet for carrying out our CTIO observations when we were unable to be present for our run. We thank Terapix, in particular Patrick Hudelot, for their help in reducing CFHT WIRCAM data. MLB would also like to thank Sean McGee for calibrating our AAT data using ASTROM-ENTRY.NET. This research has made use of the NASA/IPAC Extragalactic Database (NED) which is operated by the Jet Propulsion Laboratory, California Institute of Technology, under contract with the National Aeronautics and Space Administration. This research is supported by an NSERC Discovery grant to MLB. PM and HB acknowledge support by contract ASI-INAF I/023/05/0, ASI-INAF I/088/06/0, NASA grants NNX09AP45G and NNX09AP36G.

REFERENCES

- Andreon, S., Pelló, R., Davoust, E., Domínguez, R., & Poulain, P. 2000, *A&ASS*, 141, 113
- Bai, L., Rasmussen, J., Mulchaey, J. S., Dariush, A., Raychaudhury, S., & Ponman, T. J. 2010, *ApJ*, 713, 637
- Balogh, M. L., Babul, A., & Patton, D. R. 1999, *MNRAS*, 307, 463
- Balogh, M. L., Babul, A., Voit, G. M., McCarthy, I. G., Jones, L. R., Lewis, G. F., & Ebeling, H. 2006, *MNRAS*, 366, 624
- Balogh, M. L., Christlein, D., Zabludoff, A. I., & Zaritsky, D. 2001a, *ApJ*, 557, 117
- Balogh, M. L., McCarthy, I. G., Bower, R. G., & Eke, V. R. 2008, *MNRAS*, 385, 1003
- Balogh, M. L., Pearce, F. R., Bower, R. G., & Kay, S. T. 2001b, *MNRAS*, 326, 1228
- Beers, T. C., Flynn, K., & Gebhardt, K. 1990, *AJ*, 100, 32
- Bertin, E., & Arnouts, S. 1996, *A&AS*, 117, 393
- Bourdin, H., & Mazzotta, P. 2008, *A&A*, 479, 307
- Bower, R. G., Benson, A. J., Malbon, R., Helly, J. C., Frenk, C. S., Baugh, C. M., Cole, S., & Lacey, C. G. 2006, *MNRAS*, 370, 645
- Bower, R. G., Böhringer, H., Briel, U. G., Ellis, R. S., Castander, F. J., & Couch, W. J. 1994, *MNRAS*, 268, 345
- Bower, R. G., Castander, F. J., Ellis, R. S., Couch, W. J., & Böhringer, H. 1997, *MNRAS*, 291, 353
- Bower, R. G., McCarthy, I. G., & Benson, A. J. 2008, *MNRAS*, 390, 1399
- Colless, M., et al. 2001, *MNRAS*, 328, 1039
- Dariush, A. A., Raychaudhury, S., Ponman, T. J., Khosroshahi, H. G., Benson, A. J., Bower, R. G., & Pearce, F. 2010, *MNRAS*, 405, 1873
- Davé, R., Oppenheimer, B. D., & Sivanandam, S. 2008a, *MNRAS*, 391, 110
- . 2008b, *MNRAS*, 391, 110
- Dietrich, J. P., Biviano, A., Popesso, P., Zhang, Y., Lombardi, M., & Böhringer, H. 2009, *A&A*, 499, 669
- Donahue, M., et al. 2001, *ApJL*, 552, L93
- Eke, V. R., Baugh, C. M., Cole, S., Frenk, C. S., King, H. M., & Peacock, J. A. 2005, *MNRAS*, 362, 1233
- Eke, V. R., et al. 2004a, *MNRAS*, 348, 866
- . 2004b, *MNRAS*, 355, 769
- Gilbank, D. G., Bower, R. G., Castander, F. J., & Ziegler, B. L. 2004, *MNRAS*, 348, 551
- Giodini, S., et al. 2009, *ApJ*, 703, 982
- Gonzalez, A. H., Zaritsky, D., & Zabludoff, A. I. 2005, *ApJ*, 618, 195
- . 2007, *ApJ*, 666, 147
- Hicks, A. K., et al. 2008, *ApJ*, 680, 1022
- Hogg, D. W., Blanton, M., Lang, D., Mierle, K., & Roweis, S. 2008, in *Astronomical Society of the Pacific Conference Series*, Vol. 394, *Astronomical Data Analysis Software and Systems XVII*, ed. R. W. Argyle, P. S. Bunclark, & J. R. Lewis, 27–+
- Horner, D. 2001, PhD thesis, University of Maryland
- Hou, A., Parker, L. C., Harris, W. E., & Wilman, D. J. 2009, *ApJ*, 702, 1199
- Ikebe, Y., Reiprich, T. H., Böhringer, H., Tanaka, Y., & Kitayama, T. 2002, *A&A*, 383, 773
- Jones, D. H., et al. 2009, *MNRAS*, 399, 683
- Kochanek, C. S., et al. 2001, *ApJ*, 560, 566
- Laganá, T. F., Lima Neto, G. B., Andrade-Santos, F., & Cypriano, E. S. 2008, *A&A*, 485, 633
- Lang, D., Hogg, D. W., Mierle, K., Blanton, M., & Roweis, S. 2010, *AJ*, 139, 1782
- Lin, Y.-T., & Mohr, J. 2004, *ApJ*, 617, 879
- Lin, Y.-T., Mohr, J. J., & Stanford, S. A. 2003, *ApJ*, 591, 749
- Mazzotta, P., Rasia, E., Moscardini, L., & Tormen, G. 2004, *MNRAS*, 354, 10
- McCarthy, I. G., Babul, A., Bower, R. G., & Balogh, M. L. 2008, *MNRAS*, 386, 1309
- McCarthy, I. G., et al. 2010a, *MNRAS*, 406, 822
- . 2010b, *MNRAS*, 406, 822
- McGee, S. L., & Balogh, M. L. 2010, *MNRAS*, 403, L79
- Osmond, J. P. F., & Ponman, T. J. 2004, *MNRAS*, 350, 1511
- Popesso, P., Biviano, A., Böhringer, H., & Romaniello, M. 2007, *A&A*, 461, 397
- Popesso, P., Biviano, A., Böhringer, H., Romaniello, M., & Voges, W. 2005a, *A&A*, 433, 431
- Popesso, P., Böhringer, H., Romaniello, M., & Voges, W. 2005b, *A&A*, 433, 415
- Pratt, G. W., Croston, J. H., Arnaud, M., & Böhringer, H. 2009, *A&A*, 498, 361
- Pratt, G. W., et al. 2010, *A&A*, 511, A85+
- Ramella, M., Boschin, W., Geller, M. J., Mahdavi, A., & Rines, K. 2004, *AJ*, 128, 2022
- Rasmussen, J., & Ponman, T. J. 2007, *MNRAS*, 380, 1554
- . 2009, *MNRAS*, 399, 239
- Rasmussen, J., Ponman, T. J., Mulchaey, J. S., Miles, T. A., & Raychaudhury, S. 2006, *MNRAS*, 373, 653
- Reiprich, T. H., & Böhringer, H. 2002, *ApJ*, 567, 716
- Rozo, E., et al. 2009, *ApJ*, 703, 601
- Rykoff, E. S., et al. 2008a, *ApJ*, 675, 1106
- . 2008b, *MNRAS*, 387, L28
- Schlegel, D. J., Finkbeiner, D. P., & Davis, M. 1998, *ApJ*, 500, 525
- Sun, M., Voit, G. M., Donahue, M., Jones, C., & Forman, W. 2009, *ApJ*, 693, 1142
- Tinney, C. G., et al. 2004, in *Presented at the Society of Photo-Optical Instrumentation Engineers (SPIE) Conference*, Vol. 5492, *Society of Photo-Optical Instrumentation Engineers (SPIE) Conference Series*, ed. A. F. M. Moorwood & M. Iye, 998–1009
- Vikhlinin, A., Kravtsov, A., Forman, W., Jones, C., Markevitch, M., Murray, S. S., & Van Speybroeck, L. 2006, *ApJ*, 640, 691
- Vikhlinin, A., et al. 2009, *ApJ*, 692, 1033
- Zibetti, S., White, S. D. M., Schneider, D. P., & Brinkmann, J. 2005, *MNRAS*, 358, 949